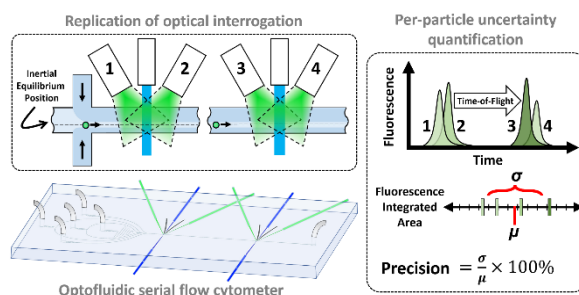


Serial flow cytometry in an inertial focusing optofluidic microchip for direct assessment of measurement variations †

Matthew DiSalvo,^{a,b} Paul N. Patrone^c, Anthony J. Kearsley,^c and Gregory A. Cooksey^{b,*}

Flow cytometry is an invaluable technology in biomedical research, but confidence in single-cell measurements remains limited due to a lack of appropriate techniques for uncertainty quantification (UQ). It is particularly challenging to evaluate the potential for different instrumentation designs or operating parameters to influence the measurement physics in ways that change measurement repeatability. Here, we report a direct experimental approach to UQ using a serial flow cytometer that measured each particle more than once along a flow path. The instrument was automated for real-time characterization of measurement precision and operated with particle velocities exceeding $1 \text{ m} \cdot \text{s}^{-1}$, throughputs above 100 s^{-1} , and analysis yields better than 99.9 %. These achievements were enabled by a novel hybrid inertial and hydrodynamic particle focuser to tightly control particle positions and velocities. The cytometer identified ideal flow conditions with fluorescence area measurement precision on the order of 1 % and characterized tradeoffs between precision, throughput, and analysis yield. The serial cytometer is anticipated to improve single-cell measurements through estimation (and subsequent control) of uncertainty contributions from various other instrument parameters leading to overall improvements in the ability to better classify sample composition and to find rare events.



Graphical Abstract We present a microfluidic serial flow cytometer that repeats measurements on flowing objects for per-object uncertainty quantification. The automated system assessed measurement precision as a function of its flow focusing operating parameters.

Introduction

Flow cytometry is essential for biomedical research, clinical applications, and the pharmaceutical industry.^{1,2} The technique relies on fluorescence-based measurements of cells labeled with fluorescent biomarkers as they cross an optical interrogation region in a flow channel. Fluorescent emissions, as well as excitation light scattered by the cells, are collected on photodetectors such as photomultiplier tubes (PMTs). The resultant signals are then analyzed to relate optical measurements to biological properties such as size, granularity, and biomarker content. The specialization of modern cytometers beyond this general approach has been driven in large part by the pressing need for better classification of complex samples, such as those that might include circulating tumor cells (CTCs).³ Recent developments in image-based, hyperspectral, and

^a Department of Mechanical Engineering, Johns Hopkins University, Baltimore, Maryland 21287, United States.

^b Microsystems and Nanotechnology Division, National Institute of Standards and Technology, Gaithersburg, Maryland 20899, United States.

^c Applied and Computational Mathematics Division, National Institute of Standards and Technology, Gaithersburg, Maryland 20899, United States.

* Corresponding author. Phone: +1 (301) 975-5529, E-mail: gregory.cooksey@nist.gov.

† Electronic Supplementary Information (ESI) available: Chip design mask; Supplemental Figures and Video

parallelized flow cytometry have sought to enhance the measurement capabilities of high-throughput cell detection.^{4–11}

Despite flow cytometry proving to be incredibly useful as a single-cell measurement tool, fundamental questions remain with respect to the impact of effects such as flow conditions and device variations on per-event measurement uncertainties. Such issues are critical for addressing subsequent problems, i.e., separating population heterogeneity from measurement variation, detecting rare events, and characterizing comparability between instruments. Moreover, theoretical uncertainty quantification (UQ) for this problem is demanding due to the interplay between measurands, fluids, light, and optics within the instrument. Traditional approaches to UQ in cytometry rely on well-defined fluorescent microspheres¹², although they still convolve population properties with flow and device-induced effects. Furthermore, the mismatch in optical and mechanical properties between fluorescent microspheres and cells calls into question their appropriateness as reference materials for uncertainty estimation. Ultimately, these observations suggest that individual cytometry measurements lack quantifiable confidence. Improvements in single cell measurements require new perspectives and technologies to estimate (and subsequently control) uncertainty contributions from various flow and other instrument parameters.

To address these problems, we consider a new type of cytometer that uses repeat interrogation of objects at multiple points along the flow path to directly assess uncertainty in individual fluorescence and scatter measurements. The key experimental technique underpinning this cytometer is the use of optofluidic fabrication approaches, which combine traditional microfluidic designs with optical waveguides and structures. The repeatability of this fabrication processes allows us to create independent but practically identical realizations of a laser interrogation region at multiple points along the flow channel, which is necessary to quantify uncertainties associated with effects arising from operating conditions. As a proof of concept, we demonstrate that this system can be used to characterize counting uncertainty due to, for example, flow focusing effects in the microfluidic channel.

Attention to flow parameters is motivated by a key challenge that arises during operation of our serial cytometer: matching repeated signals separated in time and space to their corresponding particles. At high throughputs (velocities $\approx 1 \text{ m}\cdot\text{s}^{-1}$ and event rates $> 100 \text{ s}^{-1}$) unambiguous particle tracking requires that the instrument minimizes: 1) variations in both the flow and particle velocities, which subsequently reduces the probability of particle reordering; and 2) instances of multiple occupancy within a laser interrogator (“multiplets”). As we show, satisfying these requirements entails exceptional control over particle positioning, which is itself a notable contributor to measurement variation.^{13,14} Furthermore, to ensure reliable measurements of biological phenomena such as inherent population variability, a serial cytometer must be designed to minimize all other sources of measurement variation.

The solution to the flow focusing challenge relies on leveraging the full capabilities of microfluidic lab-on-a-chip technologies.^{15–18} Traditionally, hydrodynamic focusing (HDF) is used to force a sheath fluid around the sample stream and compress particles’ positions in the flow channel (typically at the centerline).¹⁵ More recently, inertial microfluidic cytometers have demonstrated higher throughputs, smaller channel sizes, and improved velocity coefficient of variations (CVs) with little or no sheath fluids.^{9,19,20} The inertial effects on particles, which are characterized using particle-based Reynold’s number, Re_p , can result in drift of particles from their initial streamlines.^{21–24} Ultimately, the particles can become “crystallized” into narrow streams that are selectively positioned within the channel cross-section at one or more modal equilibria. Such particle configurations should be ideal for the tracking needs of a serial cytometer because they enforce uniform particle position, velocity, and ordering while minimizing probabilities of multiplets.

In this work, we present a microfabricated optofluidic serial flow cytometer that validates use of a hybrid 3-D HDF and inertial focusing approach to position particles precisely and robustly for repeated optical interrogations. This **enables the direct and quantitative characterization of variations in cytometry measurements**. The system was fully automated for throughput rates above 100 s^{-1} , and characterized measurement tracking accuracy, velocity distribution, and individual particle measurement precision under different flow conditions. By performing automated screens, we also demonstrate the robustness of the system even in low-sheath fluid flow conditions. The instrument allows the user to tune operating conditions to achieve a desired balance between measurement precision, tracking accuracy, and throughput.

Results

Serial Cytometry: Repeated Optical Measurements of Objects in Flow

A serial flow cytometer with an upstream hydrodynamic flow focusing element was designed for repeated measurement of single particles passing through multiple identical interrogation regions along a single flow path (Fig. 1A). Each region consisted of patterned waveguides coupled to fiber optics that were positioned near the flow channel. To collect measurements from different geometric perspectives, an emission waveguide was placed on both upstream and downstream side of the excitation waveguide, in epi-fluorescence configuration to reduce collection of excitation light. For simplicity, scattered light detection was performed by an obscuration-free forward-scatter waveguide that also doubled as a transmission collector. A modified excitation waveguide (Fig. 1B) was used to produce the straight and narrow beams necessary for reproducible particle illumination. Typical light beams exiting fiber-coupled waveguides are generally 1) wide and 2) naturally diverge,¹⁸ which is undesirable because of 1) the increased chance for multiple particles to occupy the beam and 2) variable excitation power and dosage for particles crossing the beam at different distances along the axis of beam propagation. To achieve more desirable optical profiles, the output beams of the excitation waveguide were filtered through a narrow opaque-walled tunnel created by a multi-layered fabrication approach (see [Materials and Methods](#)). When 10 $\mu\text{mol/L}$ fluorescein in the channels was excited at 488 nm by the modified waveguides, thin and straight excitation beams were observed with a width of $28.0 \mu\text{m} \pm 1.3 \mu\text{m}$ (unless otherwise noted, data are presented as the mean \pm one standard deviation) and divergence angle of $1.6^\circ \pm 0.2^\circ$ (both measurements taken on $N = 19$ focal planes imaged from 2 beams) (Fig. 1C).

The full serial cytometer microchip design incorporated two waveguide assemblies positioned 2.5 mm and 18.5 mm downstream of the flow focusing system (see [ESI](#) for chip design mask). The microchip was supported by arrays of automated instrumentation including syringe pumps, fiber-coupled diode lasers, fiber-coupled PMTs, silicon photodetectors (for forward scatter detection), and signal digitizers (Fig. 2A). The system recorded raw signals in 6 channels, each of which consisted of 0.5 μs resolution traces of voltage corresponding to the intensity of upstream or downstream fluorescence emission or forward scatter at one of the two interrogation regions. Peaks in these signals corresponded to the passing of individual fluorescent microspheres through optical interrogators ("events") and were unimodal in shape and approximately symmetric about the peak (Fig. 2B). In the case of scatter, peak heights are proportional to particle cross-sectional area (Fig. S1). By processing the signals with an analysis pipeline, values of *replicated* peak height, width, area, and velocity were extracted (Fig. 2C – F). Briefly: 1) signals rising above a threshold level were detected, 2) each signal was windowed to a time interval to allow the disposal of non-event data, 3) peak

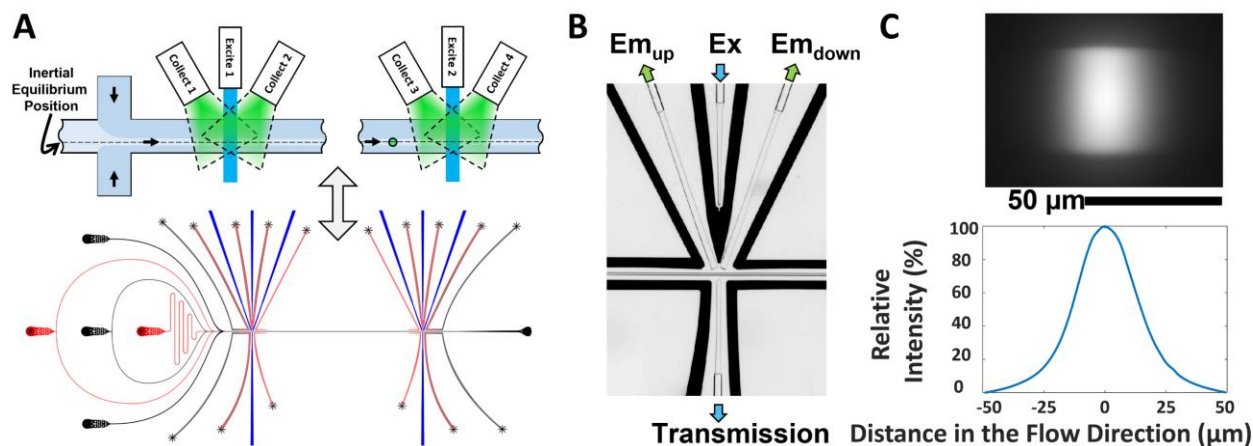


Fig. 1 Replication of optical measurements by a serial cytometer. A) Schematic and microfluidic layout of the serial cytometer. Red and black microchannels were formed in different device layers; Blue channels formed fiber-coupled waveguides. B) Brightfield microscopy image illustrating the anatomy of the optical interrogation region utilized in the serial cytometer. C) Average projection fluorescence microscopy image (top) and maximum intensity projection profile (bottom) of light emitted by a stream of fluorescein, flowing left to right, excited by a 488 nm beam in the serial cytometer.

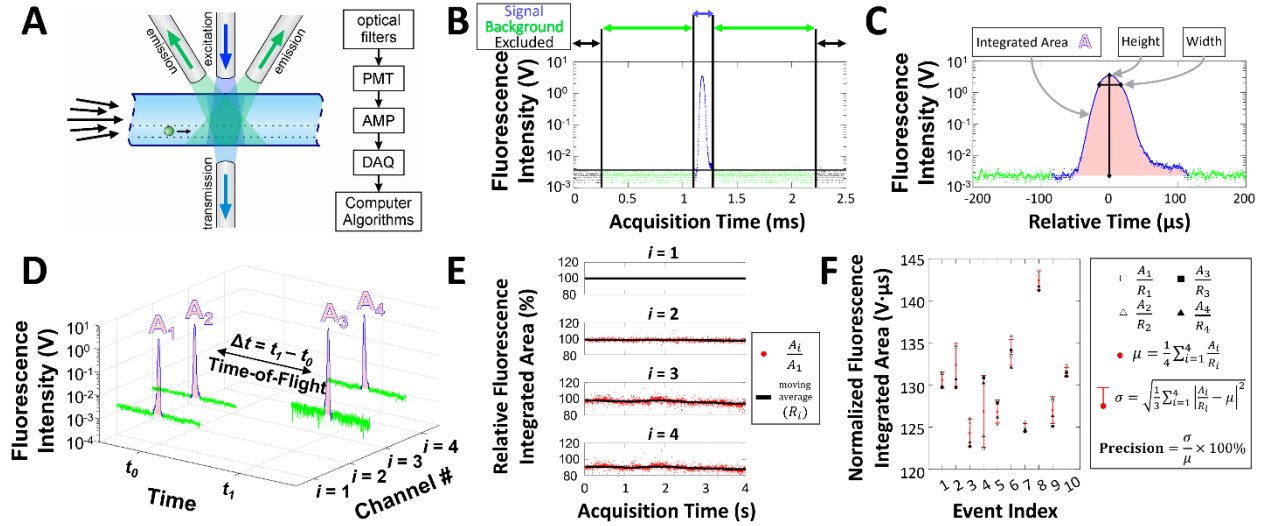


Fig. 2 Serial cytometry measurement strategy. A) Fluorescence measurement pathway ending in digitized signals. B) Thresholding and background windowing of a representative digital signal. C) Magnified view illustrating the extraction of signal integrated area, peak height, and peak width (full width at half max) from the time trace. A moving average trace is overlaid over the raw measurement samples. D) Grouping of replicated measurements of integrated fluorescence area from one particle by the time of measurement and photodetector channel number. E) Modeling of non-random differences over time between measurement channels, using channel 1 as the reference. F) Normalized serial cytometry measurements from a randomly selected series of 10 consecutive particles. Per-particle measurement precision is quantified directly from the spread of the measurement replicates.

metrics (areas, widths, and heights) were calculated, 4) steps 1-3) were repeated for each replicate measurement channel and the resulting metrics were grouped by event index to comprise replicates, and 5) replicate metrics were normalized to correct for systematic differences between photodetector channels (see [Materials and Methods](#) for details).

A Hybrid Focusing Strategy for Flow Cytometry

An important requirement for flow cytometry is the stability of spatial positioning of particles during optical interrogation. The efficiencies of illumination and photodetection, and particle-fluid, particle-channel, or particle-particle interactions depend on position of the particle in the channel. Controlling particle positioning for serial cytometry is challenging because this control needs to be maintained for the entire duration of particle transit from one optical interrogation region to another. Another consideration is that replicated signals acquired from particles must remain strongly correlated in order to accurately identify and match signals to their associated particle. As discussed in more detail below, the timing of signals is one potentially identifier but using it consistently requires stable particle velocities. Therefore, the critical design criterion for a serial flow cytometer in this work was to minimize variability in particle velocities and positions.

To provide extensive control over particle positioning, a 2-stage hybrid 3D-HDF and inertial focuser (“hybrid focuser”) was devised in a two-layer PDMS microfluidic chip ([Fig. 3A](#)). Our overall strategy blended and extended the approaches taken by Chang *et al.*, 2007 for 3D-HDF, Lee *et al.*, 2010 for sheath fluid biasing, and Oakey *et al.*, 2010 for staged focusing.^{19,20,25} Specifically, in the first stage of the device, sheath fluid was incorporated in 3-D around the sample core stream in stages using interconnecting channels, first from above, then from below, and lastly from left and right sides simultaneously. The ratio between left and right sheath fluid flow rates was biased to push particles away from the channel centerline. The second stage was a straight channel with rectangular cross-section. Thus, we adopted a focusing strategy that takes particles entering the focuser along arbitrary streamlines, uses sheath fluids to pre-position particles to approximate inertial equilibrium streamlines while simultaneously accelerating them, and rapidly equilibrates particles at one stable inertial focusing mode within the flow channel.

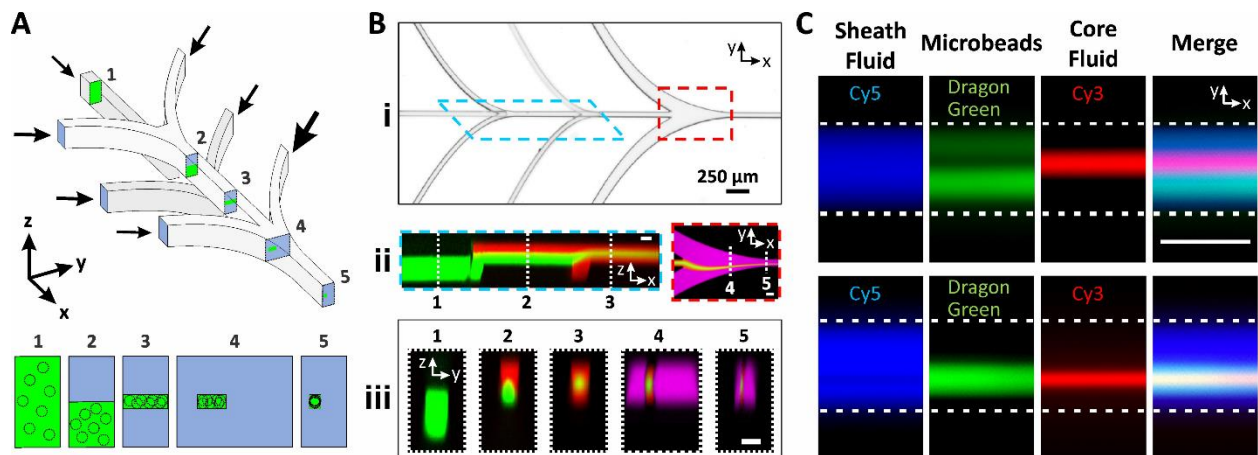


Fig. 3 Hybrid 3D-hydrodynamic and inertial particle focusing. A) Schematic of the two-layered microfluidic channels for flow focusing and five cross-sections illustrating the focusing mechanism (green: fluidic core; blue: sheath fluid; circular silhouettes: particle positions). B) Microscopy images of microfabricated flow focusing channels: i, brightfield top-down view; ii, fluorescence side and top-down views; iii, fluorescence cross-sections corresponding to the schematic in A). In the composite fluorescence images, the labeled core fluid is green, the upper and lower sheath fluids are red, and the left and right sheath fluids are magenta. C) Long-exposure fluorescence imaging of inertial equilibrium positions for particles focused by the hybrid focuser using centrally focused (top) and biased (bottom) 3D-HDF. White dashes indicate channel boundaries. All scalebars indicate the channel width, 40 μm , unless otherwise indicated.

Control of particle positioning with the hybrid focuser was assessed by optical sectioning microscopy while adjusting the flow rates of fluorescently labeled sheath and core fluids (**Fig. 3B**). The four sheath and one core fluid flow rates (totaling 59 $\mu\text{L}/\text{min}$) were calculated to target a 6.1 μm wide \times 8.9 μm high core positioned at $z = 0 \mu\text{m}$, $y = 10.2 \mu\text{m}$, which qualitatively matched the observed dimensions and validated the ability of 3D-HDF to adjust core stream position, size, and shape. The method for flow rate calculations used in all experiments of this work is detailed in **Materials and Methods: Flow Focusing Calculations**.

Next, we introduced fluorescent polystyrene microspheres (manufacturer's nominal diameter $a = 15.25 \mu\text{m}$) to a core stream with calculated 7.625 $\mu\text{m} \times 7.625 \mu\text{m}$ cross-section and used high-speed imaging to explore inertial focusing. When equal proportions of left and right sheath fluids were used (bias ratio [BR] of 1), the labeled core fluid was center-focused. The microspheres aligned with center-focused core fluid at low flow rates, but when the total flow rate was increased from 4.8 $\mu\text{L}/\text{min}$ to 59 $\mu\text{L}/\text{min}$ (equivalent to particle-based Reynolds number [Re_p] from 0.18 to 2.95), particles lost alignment with the core fluid and dynamically migrated away to either side of the center streamline (**Fig. 3C and S2**). To isolate particles to only one side of the streamline, unequal proportions between left and right sheaths were used (**Supplemental Video**). With Re_p at 2.95 and a BR of at least 1.45 (28.3 $\mu\text{L}/\text{min}$: 19.5 $\mu\text{L}/\text{min}$), the microspheres were located only on the side opposite the dominant sheath (100 % of $N = 2931$). At a BR of 5.24 (40.13 $\mu\text{L}/\text{min}$: 7.66 $\mu\text{L}/\text{min}$) the labeled core fluid was also aligned with the particle positions, which, from $x = 1 \text{ mm}$ to 2.5 mm downstream of the 3D-HDF outlet, were tightly focused at $y = +10.35 \mu\text{m} \pm 0.29 \mu\text{m}$ ($N = 203$) with a velocity CV of 0.70 %. At these conditions, we also visually confirmed the occurrence of dynamic particle-particle repulsive interactions and particle trains, consistent with other reports (**Fig. S3**).^{9,20} Particles were displaced further from the centerline at higher flow rates, up to $y = +13.89 \mu\text{m} \pm 0.49 \mu\text{m}$ at 118 $\mu\text{L}/\text{min}$ ($Re_p = 11.8$) (**Fig. S4**), validating that the microfluidics supported strong inertial effects.

Importantly, the above findings emphasize that inertial forces directly counteract attempts to centrally-focus particles using 3D-HDF at high-throughput flow rates. But by focusing particles off-axis, 2-stage hybrid focusing effectively controlled positioning at velocities exceeding 1 $\text{m} \cdot \text{s}^{-1}$. Notably, the 2.5 mm flow length examined here were shorter than the $\approx 1 \text{ cm}$ length expected at this Re_p for straight channel equilibration without pre-focusing.^{19,20,24} The hybrid focusing results indicated that pre-focusing particles deterministically selected for a single inertial node and suggested an acceleration of the inertial equilibration process.

Validation of serial cytometry

Variations in replicate measurements were quantified as precision, defined to be the ratio of standard deviation to the mean of normalized replicated measurements (i.e., the replication¹ coefficient of variation). The normalization estimated, and accounted for, systematic biases and non-random differences between measurement channels. As a result, the reported measurement precision primarily describes random effects. For proof-of-concept, measurement precision and population measurement variations were obtained for fluorescent microspheres focused by three different particle focusing strategies. To test focusing by traditional 3D-HDF, similar conditions to the preliminary imaging experiments were used: Re_p values were set to 3.3 or 0.5, Sheath-to-core ratio (SCR) was set to 54, and BR was set to 1 to centrally focus the particles. Then, hybrid focusing to a single node was performed with $Re_p = 3.3$, $SCR = 54$, and $BR = 7.8$. The results (Fig. 4 and Table 1) showed differences in the ability of the cytometer to reproducibly measure fluorescence and scatter values. The improvements to fluorescence area precision and velocity CV for hybrid focusing were consistent with this method's enhanced stability in particle positioning seen in the imaging studies. The distributions of fluorescence measurement precision were substantially skewed, with some particles measured more than tenfold less reproducibly than the population median. As further validation, the particles were assessed by a commercial cytometer, resulting in a fluorescence area CV of 10.74 % and forward scatter area CV of 4.17 %, which were consistent with Table 1 and the manufacturer-specified diameter variability of 4.4 %. Overall, these results demonstrated the feasibility of assessing measurement precision for cytometry and showed that changes in precision reflected changes in inertial flow phenomenon observed by imaging and velocimetry. This experimental data validated the theoretical link between measurement reproducibility and accuracy in estimated population-level variations.

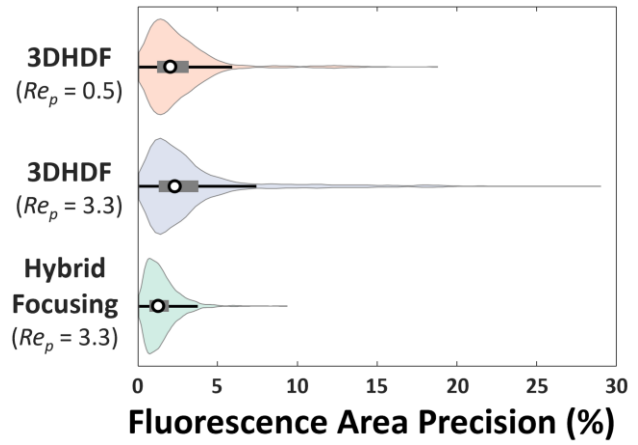


Fig. 4 Distributions of precision in measurements of fluorescence area from individual microspheres evaluated at three different flow conditions. Violin plots represent kernel density estimates and are overlaid with box-and-whisker plots. Gray boxes represent the interquartile range (IQR); white circles indicate the median; black lines extend $1.5 \times IQR$.

Table 1. Effect of particle focusing on population variations and measurement precision for fluorescence, forward scatter, and velocity.

	Fluorescence-Area CV (%)	Median Fluorescence-Area Precision (%)	Forward Scatter-Height CV (%)	Median Forward Scatter-Height Precision (%)	Velocity CV (%)	Median Velocity Precision (%)	Sample Size
3D-HDF ($Re_p = 0.5$)	$10.15 \pm 0.25^*$	2.03 ± 0.07	4.35 ± 0.11	1.46 ± 0.07	5.62 ± 0.14	0.0054 ± 0.0020	816
3D-HDF ($Re_p = 3.3$)	10.33 ± 0.18	2.30 ± 0.05	5.49 ± 0.10	2.91 ± 0.07	0.46 ± 0.01	0.0060 ± 0.0002	1609
Hybrid focusing ($Re_p = 3.3$)	9.64 ± 0.17	1.20 ± 0.02	4.30 ± 0.08	1.58 ± 0.06	0.20 ± 0.01	0.0060 ± 0.0002	1718

* Metrics are reported \pm standard error.

¹ The fluorescence signals are more precisely described as a collection of pairs of measurements that are: (i) independent between pairs by virtue of being at different laser regions; and (ii) dependent within a pair because the corresponding signals are generated by the same laser (although the detectors and geometric factors are different).

Ultra-precise real-time signal matching

The above preliminary serial cytometry experiments were performed at relatively low event rates to unambiguously match signals to their particles. More specifically, matching was facile when particle time-of-flights (TOFs) were brief and particle spacings were large (see top panel of Fig. 5A). For example, 81 % matching yield was achieved by filtering unambiguous matches from data collected under the aforementioned 3D-HDF focusing condition with a particle event rate of 1.5 s^{-1} . However, at a particle velocity of $0.75 \text{ m}\cdot\text{s}^{-1}$, TOFs in the serial cytometer were sufficiently long (approximately 20 ms) that at higher throughputs and shorter interparticle spacing signal matching became non-trivial (Fig. 5B). The combined low measurement throughput and low tracking yields would severely limit the usefulness of the serial cytometer. Thus, we explored a more sophisticated matching approach for serial cytometry.

To match objects from data acquired under high throughput conditions, the matching method included two components: 1) build (or regularly update) a prediction model of particles' TOFs, and 2) for each particle, use its predicted TOF to establish a relative timeframe that estimated arrival times at all measurement channels (see bottom panel of Fig. 5A). The implementation of the method, termed here as "Forward-Projection Time Subdivision" (FPTS), is described further in Materials and Methods. The predictive model did not rely on any *a priori* information; instead, the initial TOFs were estimated from the time-shift in arrival patterns between channels. By periodically updating the predictive model for FPTS, the method was designed to track particles despite velocity variations that may occur in the cytometer due, for instance, to flow rate oscillations or to changes in flow rates by the operator.

To characterize the FPTS method, tracking yields were assessed in data acquired from the fluorescent microspheres by the serial cytometer at various operating conditions. The data were obtained with different particle concentrations, core flow rates, and focusing approaches to produce a range of latencies (1 ms to 10 ms) and variations in TOF (25 μs to 700 μs) with at least 10 000 particles measured per condition (Fig. 5C). FPTS tracking yields were correlated with both particle population velocity variations and particle event rates. When velocity variations were minimized using the hybrid particle focusing strategy, the best FPTS tracking yield was 99.94 % (95 % C.I. [99.93 % to 99.96 %]). For all conditions, the matching was computed in under 100 ms, which facilitated real-time particle tracking by the automation theme (Fig. S5). The real-time analysis allowed the cytometry system to provide active feedback on measurement precision and particle focusing. The highest tested event rate that was analyzed in real-time was 787 s^{-1} . Further examination of the data, alongside imaging validations, showed that signals that were unable to be matched using FPTS followed a pattern (Fig. S6): close particles that were coincident within one laser interrogator, but separate in the other laser region, resulted in a net "deletion" of one or more of the well-resolved particles.

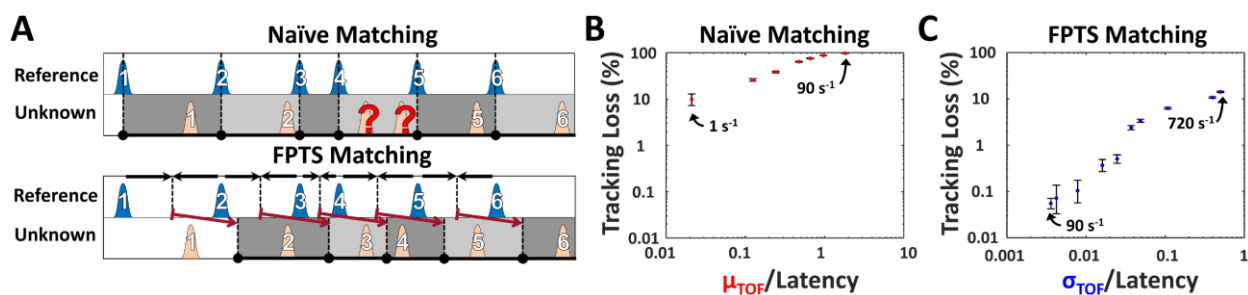


Fig. 5 Particle tracking methods for serial cytometry. A) Schematics for tracking methods. A naïve approach matches unknown signals to the reference only when the time-of-flight (TOF) was less than the latency. The FPTS approach matches based on predicted time-of-flight (Red arrows). B-C) Tracking losses in serial cytometry using the naïve approach or FPTS approach. Datapoints and error bars represent the mean and 95 % confidence intervals (Clopper-Pearson binomial proportion intervals). Red and blue colors emphasize that B) scales with mean TOF (μ_{TOF}) whereas C) scales with the standard deviation of TOF (σ_{TOF}). Arrows indicate the serial cytometer's event rates for selected conditions.

Feedback control of the serial cytometer

The real-time analysis and high-throughput capabilities of the serial cytometer enabled the system to provide rapid feedback on changes to its own flow parameters. To realize this in practice, we characterized relationships between fluorescence measurement precision, flow rates, and particles sizes. Three parameters of interest were considered in order: particle-based Reynolds number Re_p , lateral hydrodynamic stream position y_{core} , and sheath-to-core ratio (SCR). The automated system tested 29 flow conditions across feasible ranges of the three parameters (Table S1) with a size mixture (15 μm , 7 μm , and 4 μm nominal diameter) of fluorescent microspheres, assessing fluorescent area precision over more than 150 000 particles in total. The test revealed opportunities to improve fluorescent measurement precision, particularly with the largest 15 μm particles (Fig. 6A). First, fluorescent measurement precision improved substantially as Re_p increased from 0.4 to 6, suggesting that faster inertial equilibrations of the particles enhanced measurement repeatability. Next, precision at $Re_p = 6$ was sensitive to core placement y_{core} with optimal placement 60 % between the channel centerline and the channel wall opposite the laser. With these two refinements, precision was insensitive to SCR. For the smaller 7 μm or 4 μm particles (Fig. S7), $Re_p < 1$ for most conditions, and precision was generally sensitive only to the SCR. This behavior was characteristic of 3D-HDF under Stokes flow and reflected minimal benefits from inertial effects at these conditions. For all particles, the trends in precision agreed with trends in the CVs of particle velocities (Fig. S8), reaffirming particle focusing as a driving mechanism for the changes in precision in this study. Overall, these results showed that relatively little sheath fluid was required to consistently focus particles at high Re_p and provide further evidence that the channel centerline was a particularly unstable position for particles.

Based on these results, low-variation conditions were identified for 15 μm microspheres. At Re_p of 6 and y_{core} of 0.6, the SCR was adjusted between 3 and 80 in twelve increments to demonstrate tunability in event rates between 5 s^{-1} to 495 s^{-1} from a sample concentration of 10^6 particles mL^{-1} . This tuning increased system throughput while

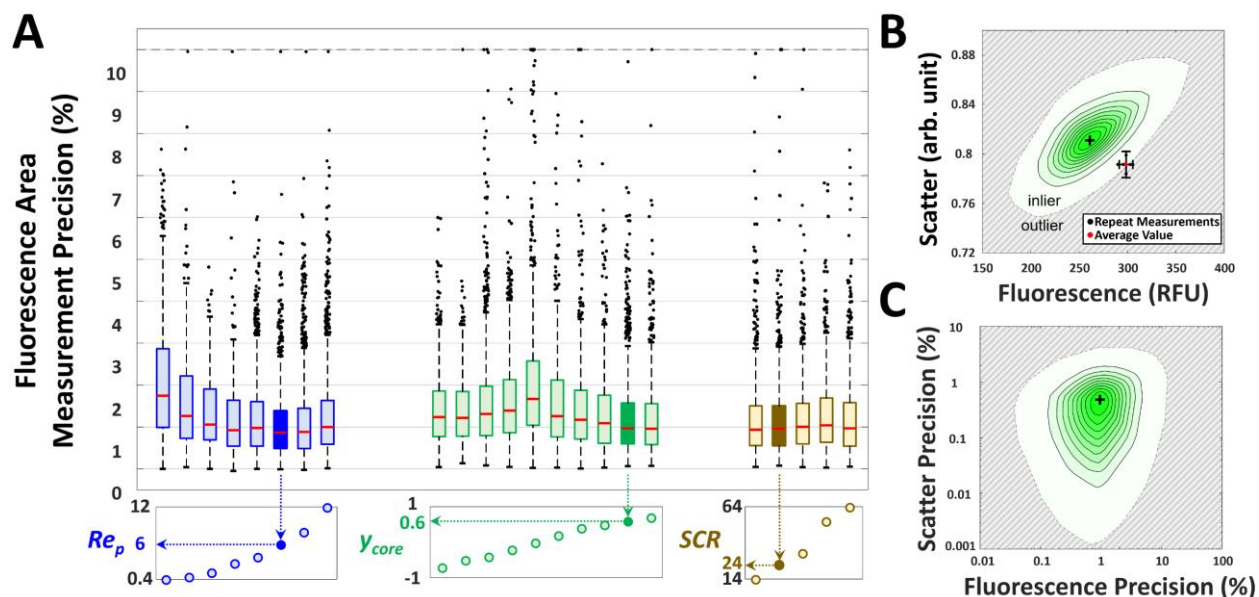


Fig. 6 Refinement of measurement precision through serial cytometry evaluations of flow focusing parameters. A) Representative box-and-whisker plots illustrating the optimization of precision in fluorescence measurements of 15 μm fluorescence particles through sequential evaluation of three flow parameters: Re_p , y_{core} , and SCR. Colored boxes represent the interquartile range (IQR); red lines indicate the median; dashed black lines extend $1.5 \times \text{IQR}$. For visibility, the y-axis is clipped at the dashed line and only outlier measurements are drawn. B-C) Serial cytometry contour density plots. Contours represent deciles for data ranked by bivariate adjusted outlyingness; outermost contour represents the outlier threshold. "+" indicates the Tukey median. B) Sample population density in forward scatter height and fluorescence area. For clarity only one point is shown with estimates of precision. C) Sample population density in precision for the same measurements as B).

maintaining median fluorescence area precision $< 1.8\%$, particle population velocity CV $< 0.25\%$, and tracking yield $> 99.5\%$. The best precision with the serial cytometer was achieved with a SCR of 20, when the median fluorescence area and scatter height measurement precisions were 0.93% and 0.50% . The particles in this condition were tightly focused, with particle population velocity of $0.759 \text{ m}\cdot\text{s}^{-1} \pm 1.45 \text{ mm}\cdot\text{s}^{-1}$ (95 % C.I. for the coefficient of variation of velocity: $[0.17\% \text{ to } 0.25\%]$) that enabled a particle tracking rate of 99.95% from a total count of 112 307 microspheres at an average event rate of 93 s^{-1} . For consistency with traditional flow cytometry studies, this dataset could be represented in contoured densograms with boundaries gating the population (Fig. 6B). However, it is important to reiterate that serial cytometry additionally produced, *on a per particle basis*, repeated cytometry measurements (scatter points in Fig. 6B) allowing the quantification of precision (Fig. 6C). These results demonstrated the utility of serial cytometry to refine sample- and instrument-dependent operating parameters and illustrated the expanded dimensionality of data produced by the instrument.

Discussion and Conclusions

The fluidic aspects of flow cytometers are key to the ability of these instruments to take cellular measurements. There are several approaches to control flow, but to the best of our knowledge there is no systematic study of their impacts on the measurement process. Given their potential for introducing variability it is critical to understand links between the physics of microflows and UQ in cytometry.

To explore these links, it was necessary to decouple flow-related variations from population-level heterogeneity. Solving this problem by experimental techniques entailed tracking and repeating measurement of individual particles. This enabled UQ *on a per particle basis* which isolates effects associated with the instrument and enables quantitative cell classification. For our cytometer this UQ indicated an average baseline of $\approx 1\%$ relative variation in fluorescence measurement due to instrumentation. Increases in relative variations were observed when flow conditions were changed, thereby quantifying flow-related effects on measurement repeatability. This ability to quantify uncertainty due to flow effects allows for subsequent optimization of device operation.

Historically, device operation has been driven by throughput needs alone without fully considering the additional interplay between flow parameters and accuracy. Hydrodynamic focusing has generally been considered a means to control position, but as our work shows, it can significantly impact uncertainty. Furthermore, strategies to increase throughput typically involve faster sample flow rates, which can increase variability simply by spreading particles across a larger cross-sectional area in the channel. Inertial effects also increase with flow rate, but their impacts on measurements are unexplored. Indeed, these effects may be counteracting hydrodynamic focusing (as we observed) and account for the unexpectedly high population CVs collected by commercial instruments using high flow rates. Given the immense ranges of biological particle sizes and velocities of interest to cytometry, it is likely impractical to universally ignore inertial aspects in such a measurement system.

The benefits of considering the role of flow have allowed us to synergize 3D-HDF with inertial focusing effects, thereby conferring several advantages for flow cytometry. First, we achieved exceedingly low particle velocity CVs below 0.2% for monodisperse particles, likely approaching the stability limits of syringe pumps. These CVs reflected tight focusing and were observed with only 2.5 mm of the channel footprint devoted to inertial equilibration. Second, the system minimized use of sheath fluid because 3D-HDF was only needed to pre-focus particles in preparation for subsequent inertial focusing. The quantity of sheath fluid was decoupled from focusing tightness, so long as the sample stream was biased away from the centerline and the first measurement regions was sufficiently downstream for particle positioning to stabilize under inertial effects. The minimum sheath fluid was substantially less than what is needed for pure HDF (SCR reduced from 100:1 to 3:1). Third, by aligning the 3D-HDF to the inertial equilibrium position, the hybrid focuser maintained a characteristic position roughly halfway between the channel center and wall regardless of particle size or velocity. This redundancy made hybrid focusing well-suited to mixtures of different particles (i.e., $4 \mu\text{m}$ versus $15 \mu\text{m}$ particles) even when subpopulations experienced substantially different inertial effects. Our physics-informed flow control strategy produced even tighter distributions in particle velocities and measurements at higher flow rates, which allowed increases in throughput to proceed together with improvements in particle focusing and measurement reproducibility. We

acknowledge that the performance of hybrid focusing may change depending on particle behaviors in flow but emphasize that the serial cytometry workflow allows for quantitative comparison of UQ against other performance metrics, which opens the possibility for refining flow focusing on a case-by-case basis (as we have demonstrated here with solid microspheres).

We note that to evaluate and refine the serial cytometer, we first needed to quantify uncertainty due to flow; yet this required being able to repeat measurements, i.e., using the serial cytometer itself. This circularity enables systematic evaluation of the increasingly complicated interplay between different physical phenomenon as one attempts to increase the accuracy of a cytometer. For example, even with our flow control strategy, we discovered that to track particles at high-throughput it became necessary to solve a signal-matching subproblem. We demonstrated a first-order solution for matching based on signal timing that sufficed for 99.9 % of matches at an event rate of 100 s^{-1} . Matching is a unique classification problem for the serial cytometer, but signals that fail to be matched highlight broader classification problems important to cytometry such as doublet detection. Additional progress in analytical theory is needed to improve doublet detection which would improve both classification in conventional cytometry and matching in serial cytometry. For example, signal shape would be valuable for doublet detection and separation but is discarded by commercial instruments.

Our study with serial cytometry questions how the measurement of analytes by flow cytometry can be limited by physics-mediated phenomenon. To answer such questions, it would be beneficial to establish a rigorous UQ for cytometry rooted in an understanding of the underlying physics. Serial cytometry represents a first step on the path. Indeed, we believe that prior to this study metrics such as tracking yield – a means of validating counting – and measurement precision – a means to compare significance between individual cytometry measurements – were undefined. The serial cytometer’s unprecedented ability for self-assessment of measurement variations is highly relevant for unpredictable samples, such as cells, where the sample’s behavior and interaction with measurement performance is unknown. Studying measurement variations arising from cellular properties, such as biomarker density, and deeper examinations of outliers is important future work. For example, serial cytometry can be used to quantify the inflation of apparent biological heterogeneity due to measurement variations. This information would inform probabilistic methods for improved classification or enumeration of cellular subpopulations. An immediate next step towards biological applications, which often have much lower optical signals, is an additional characterization of the serial cytometer’s dynamic range and limit of detection. We anticipate the knowledge gained about the precision of optofluidic measurements systems will also broadly benefit technologies and approaches outside the field of cytometry, especially high-throughput flow systems, such as velocimeters and droplet microfluidics.

Materials and Methods

Reagents

15.25 μm , 7.32 μm , 4.19 μm nominal diameter Dragon Green fluorescent microspheres were procured from Bang’s Labs (#FSDG009, #FSDG007, #FSDG006, respectively)². Triton X-100 Surfact-Amps was obtained from ThermoFisher (#28314). Sulfo-Cyanine3 carboxylic acid (#21390) and Sulfo-Cyanine5 carboxylic acid (#23390) were obtained from Lumiprobe.

Microfabrication and Microdevice Preparation

Microfluidic device layers were fabricated using soft lithographic molding of PDMS (Sylgard 184, Dow Corning) from photoresist-on-silicon master templates. The channel-facing sides of each layer were contact-printed with PDMS crosslinker to form a thin coating; the two faces were manually aligned under a

² The full description of the procedures used in this paper requires the identification of certain commercial products and their suppliers. The inclusion of such information should in no way be construed as indicating that such products or suppliers are endorsed by the National Institute of Standards and Technology (NIST) or are recommended by NIST or that they are necessarily the best materials, instruments, or suppliers for the purposes described.

microscope, and the crosslinker was cured for 1 h at 60 °C to permanently bond the device layers. As described previously, light-blocking channels were filled with opaque PDMS (Sylard 170, 1:1, Dow Corning) and multimode optical fibers for detection (numerical aperture [NA] of 0.22, 105 µm core size) and excitation (0.1 NA, 105 µm core size) were integrated into waveguides using optical adhesive (refractive index 1.56 when cured).¹⁸ The optical adhesive was cured by 1 h of full-chip exposure to UV light (100 W longwave 365 nm UV lamp) followed by 4 minutes of UV laser light (375 nm diode laser, 60 mW nominal power) directed through the waveguide. Inlet and outlet reservoirs were connected to syringe pumps (30 µm/min minimum pulse-free actuation speed) via tubing connected to biopsy-punched chip inlets by blunt needles with 90° bends. Pumps were connected by fluorinated ethylene-propylene tubing (0.762 mm inner diameter, 1.58 mm outer diameter) sheathed within flexible polymer tubing (1.58 mm inner diameter, 3.175 mm outer diameter) to provide a balance between low compliance and vibrational dampening.

Serial Cytometer Signal Acquisition, Signal Processing, and Data Analysis

Fluorescence emissions from particles excited by a blue laser (488 nm diode laser, 200 mW nominal power, 0.5 % stability over 8 h, 0.2 % RMS noise) were filtered by bandpass filters (40 nm bandpass centered at 520 nm) and detected by amplified photomultiplier tubes (H11903-20 detector, Hamamatsu). Transmitted light was directly detected by silicon photomultipliers (± 2 % uniformity, ± 0.5 % linearity). Fluorescence and transmission signals were digitized by a data acquisition card (8 analog inputs, 16 bit resolution) operating in continuous data streaming mode at a sampling rate of 2×10^6 s⁻¹ with a 4-second streaming cycle to a workstation computer. Equipment was interfaced using either the manufacturers' software developer kits or open-source MicroManager software.

Incoming digitized data streams were truncated to segments containing "peaks", defined as data segments in which any signal rises above a threshold value for at least 10 consecutive microseconds. A per-channel threshold was defined as the background level plus a consistent estimator of standard deviation of the noise. Specifically, letting X_1, X_2, \dots be measurements of the background, $\hat{\sigma} = k \cdot \text{median}(|X_i - \text{median}(X)|)$. Assuming the signal is normally distributed, the scale factor k is given by $1/(\Phi^{-1}(3/4)) \approx 1.4826$, where Φ denotes the cumulative distribution function of the standard normal distribution. Each supra-threshold peak segment was expanded by an additional 10 segment-widths to define "background" signal flanking the peak. Any overlap between the adjacent peaks' backgrounds was evenly divided. Event data was logged to hard disk drive storage in 16 bit integer format using the Hierarchical Data Format version 5 using a chunk size of 800 kilosamples.²⁶ The remaining non-event data was discarded.

For the extraction of heights, width, etc., signals were first smoothed by an unweighted moving average with centered window size equal to 4 % of the duration of "peak"-labelled data, i.e., suprathresholded portion. The background level was defined by the median of the remaining data. The signal height and time were defined as the maximum difference between the signal and background level and the corresponding time of the maximum smoothed signal value. The area under the curve was defined as the sum of the background-subtracted unsmoothed signal over the smallest continuous time interval over which the smoothed signal, included the peak, remained above the background level. The width was defined as the duration between the first and last points at which the smoothed signal crossed 50 % of the difference of the maximum smoothed signal value and the background level, using linear interpolation to calculate threshold crossings.

Signal matching was performed using TOF information. In a naïve approach to particle matching, unambiguous matching proceeded only if the TOF was less than interparticle latency. In contrast, for forward-projection time subdivision (FPTS), a particle was matched if, for each of K non-reference signal channels, there existed exactly 1 index m_k where the peak time $t_{m_k,k}$ landed between two sequential time boundaries $b_{n,k}$:

$$\forall k, \exists! m_k \mid t_{m_k,k} \in [b_{n-1,k}, b_{n,k}) \quad (1)$$

$$b_{n,k} = \begin{cases} t_{n,k_{ref}} + \frac{t_{n+1,k_{ref}} - t_{n,k_{ref}}}{2} + \delta_{n,k}, & n < N \\ \infty, & n = N \end{cases} \quad (2)$$

for $m, n \in S_1 \equiv \{1, 2 \dots, N\}$, $k \in S_2 \equiv \{1, 2 \dots, K\}$, where the boundaries $b_{n,k}$ divided time between particles into windows shifted by estimated TOFs $\delta_{n,k}$ and peak times $t_{n,ref}$ from the reference channel. In cases where multiple particles occupied a single time interval, we matched assuming order was preserved. This modification allowed correct ordering of some signals that fell outside their projected intervals without violating surrounding signal matches. Estimates of expected TOF $\delta_{n,k}^*$ for equation (1) were initialized by pattern-matching 4 s segments of newly acquired signals. Patterns were constructed by aggregating peak timings across bins of size equal to the average peak duration. The patterns were smoothed by convolution with the kernel $[1, 2, \dots, k-1, k, k-1, \dots, 2, 1]/k^2$ with $k = 80$. The local TOF shift δ between reference and unknown digitized signals was then computed directly from the patterns using cross-correlation.²⁷ If the maximum normalized correlation for a window was below 0.6, the TOF shift of the nearest window with correlation above 0.6 was used.

After matching signal replicates, height and area measurements in each channel were normalized by models of channel-to-channel differences in fluorescence intensity. The model was a moving average of the ratio of measurements in one channel to the reference channel, using a window size equivalent to 60 s. Measurement precision was defined as the ratio of the standard deviation of normalized replicates to the average of normalized replicates.

For serial cytometry experiments, extreme outliers (typically comprising < 1 % of particles, and included multiplet and/or aggregated particles) were excluded from all analyses. These outliers were detected automatically by a nonparametric metric, adjusted outlierness²⁸, which was computed from the dimensions of fluorescence peak area, scatter peak height, and velocity. For experiments with mixtures of particles, manual gating off FSC-H was first used to exclude multiplets and aggregates, followed by k-means++ clustering²⁹ to isolate the individual particle subpopulations. All reported event rates were calculated as averages taken over the full experiment duration, and counted only singlet events excluding noise, debris, and multiplets.³⁰ The standard error in population metrics were obtained by bootstrap sampling with replacement, with the exception of the coefficient of variation metric whose theoretical standard error was estimated as: $SE_{CV} \approx \sqrt{(CV^2/2 + CV^4)/N}$, where CV was the measured coefficient of variation metric and N was the sample size.

Conventional Cytometry

Mixtures of fluorescence microspheres were analysed on a conventional cytometer (50 mW laser excitation at 488 nm, peristaltic pumps, avalanche photodiodes for fluorescence and silicon photodiode for forward scatter) using data in forward scatter (FSC) and fluorescein (FITC) channels. A neutral density filter with optical density (OD) of 1 was inserted in the FITC emission path to prevent saturation of the FITC measurements at the lowest gain setting. Stock solutions of particles were diluted and mixed to produce roughly equal distribution of particles sizes at a total event rate of approximately 100 s^{-1} . Bead populations were gated by hand using both FSC and FITC channels. Statistics for median and CV for height (i.e., FSC-H) and area (i.e., FSC-A) for each channel were recorded at the lowest flow rate ($10 \mu\text{L}/\text{min}$).

Microscopy

Fluorescence microscopy images were acquired on an inverted epifluorescence widefield microscope with LED illumination. A CMOS camera (pixel size of $3.45 \mu\text{m}$, framerate of 20 s^{-1} , 14 bit resolution) was used to acquire low-framerate and structured illumination optical sectioning images. A high-framerate CMOS camera (pixel size of $6.5 \mu\text{m}$, framerate of 20500 s^{-1} for each 4 columns of pixels, 16 bit resolution) was used for videography. Cropped videoframes containing particles were triggered for acquisition by their summed fluorescence intensities. Particles' positions in images were quantified using intensity weighted centroids.

Flow Focusing Calculations

For a channel with dimensions H and W and flows rates Q_{top} , Q_{bottom} , Q_{left} , Q_{right} , Q_{core} summing to Q_{total} , the sheath-to-core ratio is defined as:

$$SCR = \frac{Q_{\text{core}}}{Q_{\text{top}} + Q_{\text{bottom}} + Q_{\text{left}} + Q_{\text{right}}} \quad (3)$$

If the flow profile in the channel is approximated to be constant, the core stream dimensions w_{core} and h_{core} were defined from the desired core aspect ratio (AR) by:

$$w_{core} = \sqrt{\frac{WH}{AR(1+SCR)}} \quad (4)$$

$$h_{core} = w_{core}AR \quad (5)$$

The particle-based Reynold's number Re_p was defined as

$$Re_p = Re \left(\frac{a}{D_h} \right)^2 = \frac{\rho U_{max} D_h}{\mu} \left(\frac{a}{D_h} \right)^2 = \frac{\rho Q_{total} D_h}{A \mu} \left(\frac{a}{D_h} \right)^2 \quad (6)$$

where $D_h = \frac{4A}{P}$ is the hydraulic diameter, ρ is the density of the fluid (0.998 kg/L) and μ is the dynamic viscosity (0.001002 Pa·s for water at 20 °C), A is the channel cross-sectional area, P is the channel perimeter, and U_{max} is the maximum flow velocity, which, for channel dimensions $W = 40 \mu\text{m}$ and $H = 80 \mu\text{m}$, was approximated as $2.19 \times U_{ave}$.³¹ The streamline aligned to the centroid of the core was defined in terms of coordinate position relative to the channel centerline as (y_{core} , z_{core}). Given desired y_{core} , z_{core} , Re_p , SCR , and AR , all experimental volumetric flow rates were calculated from the below system of equations:

$$Q_{total} = Re_p \frac{A \mu}{\rho D_h} \left(\frac{D_h}{a} \right)^2 \quad (7)$$

$$Q_{core} = \frac{Q_{total}}{1+SCR} \quad (8)$$

$$Q_{left} = \frac{Q_{total}(W+2y_{core}-w_{core})}{2W} \quad (9)$$

$$Q_{right} = Q_{total} \left(1 - \frac{w_{core}}{W} \right) - Q_{left} \quad (10)$$

$$Q_{bottom} = Q_{core}(H + 2z_{core} - h_{core})/2h_{core} \quad (11)$$

$$Q_{top} = Q_{core} \left(\frac{H}{h_{core}} - 1 \right) - Q_{bottom} \quad (12)$$

Alternatively, known volumetric flow rates Q_{total} , Q_{left} , Q_{right} , Q_{top} , and Q_{bottom} were used to estimate the core stream parameters:

$$w_{core} = W \frac{Q_{bottom}+Q_{top}+Q_{core}}{Q_{total}} \quad (13)$$

$$h_{core} = H \frac{Q_{core}}{Q_{bottom}+Q_{top}+Q_{core}} \quad (14)$$

$$y_{core} = \frac{W \left(\frac{2Q_{left}}{Q_{total}} - 1 \right) + w_{core}}{2} \quad (15)$$

Author Contributions

Conceptualization, M.D., P.N.P., and G.A.C.; Methodology, M.D. and G.A.C.; Software, M.D.; Investigation, M.D.; Resources, P.N.P. and G.A.C.; Writing – Original Draft, M.D.; Writing – Review & Editing, M.D., P.N.P., A.J.K., and G.A.C.; Supervision, G.A.C.; Funding Acquisition, P.N.P., A.J.K., and G.A.C.

Conflicts of interest

G.A.C., P.N.P., and A.J.K. are included in Patent Application 20210302300 (“Serial Flow Cytometry”).

Acknowledgements

The authors acknowledge Stephen E. Meek for providing microfabrication equipment training. M.D. was supported by a Johns Hopkins-NIST PREP Consortium fellowship and by a National Research Council fellowship. Portions of this work were conducting at the NIST Center for Nanoscale Science and Technology.

References

- 1 A. Adan, G. Alizada, Y. Kiraz, Y. Baran and A. Nalbant, *Critical Reviews in Biotechnology*, 2017, **37**, 163–176.
- 2 A. Vembadi, A. Menachery and M. A. Qasaimeh, *Frontiers in Bioengineering and Biotechnology*, 2019, **7**, 147.
- 3 R. Vaidyanathan, R. H. Soon, P. Zhang, K. Jiang and C. T. Lim, *Lab on a Chip*, 2018, **19**, 11–34.
- 4 K. O'Neill, N. Aghaeepour, J. Špidlen and R. Brinkman, *PLOS Computational Biology*, 2013, **9**, e1003365.
- 5 S. Stavrakis, G. Holzner, J. Choo and A. deMello, *Current Opinion in Biotechnology*, 2019, **55**, 36–43.
- 6 K. Goda, A. Ayazi, D. R. Gossett, J. Sadasivam, C. K. Lonappan, E. Sollier, A. M. Fard, S. C. Hur, J. Adam, C. Murray, C. Wang, N. Brackbill, D. Di Carlo and B. Jalali, *Proceedings of the National Academy of Sciences*, 2012, **109**, 11630–11635.
- 7 A. Isozaki, H. Mikami, H. Tezuka, H. Matsumura, K. Huang, M. Akamine, K. Hiramatsu, T. Iino, T. Ito, H. Karakawa, Y. Kasai, Y. Li, Y. Nakagawa, S. Ohnuki, T. Ota, Y. Qian, S. Sakuma, T. Sekiya, Y. Shirasaki, N. Suzuki, E. Tayyabi, T. Wakamiya, M. Xu, M. Yamagishi, H. Yan, Q. Yu, S. Yan, D. Yuan, W. Zhang, Y. Zhao, F. Arai, R. E. Campbell, C. Danelon, D. di Carlo, K. Hiraki, Y. Hoshino, Y. Hosokawa, M. Inaba, A. Nakagawa, Y. Ohya, M. Oikawa, S. Uemura, Y. Ozeki, T. Sugimura, N. Nitta and K. Goda, *Lab on a Chip*, 2020, **20**, 2263–2273.
- 8 K. Huang, H. Matsumura, Y. Zhao, M. Herbig, D. Yuan, Y. Mineharu, J. Harmon, J. Findinier, M. Yamagishi, S. Ohnuki, N. Nitta, A. R. Grossman, Y. Ohya, H. Mikami, A. Isozaki and K. Goda, *Lab on a Chip*, 2022, **22**, 876–889.
- 9 S. C. Hur, H. T. K. Tse and D. Di Carlo, *Lab on a Chip*, 2010, **10**, 274–280.
- 10 B. K. McKenna, J. G. Evans, M. C. Cheung and D. J. Ehrlich, *Nature Methods* 2011 8:5, 2011, **8**, 401–403.
- 11 M. Cheung, J. J. Campbell, L. Whitby, R. J. Thomas, J. Braybrook and J. Petzing, *Cytometry Part A*, 2021, **99**, 1007–1021.
- 12 R. A. Hoffman and J. C. S. Wood, *Current Protocols in Cytometry*, 2007, **40**, 1–18.
- 13 P. Ubezio and A. Andreoni, *Cytometry*, 1985, **6**, 109–115.
- 14 H. Daguerre, M. Solsona, J. Cottet, M. Gauthier, P. Renaud and A. Bolopion, *Lab on a Chip*, 2020, **20**, 3665–3689.
- 15 M. E. Piyasena and S. W. Graves, *Lab on a Chip*, 2014, **14**, 1044–59.
- 16 C. E. Sims and N. L. Allbritton, *Lab on a Chip*, 2007, **7**, 423–440.
- 17 D. Huh, W. Gu, Y. Kamotani, J. B. Grotberg and S. Takayama, *Physiological Measurement*, 2005, **26**, R73–R98.
- 18 G. A. Cooksey, P. N. Patrone, J. R. Hands, S. E. Meek and A. J. Kearsley, *Analytical Chemistry*, 2019, **91**, 10713–10722.
- 19 J. Oakey, R. W. Applegate, E. Arellano, D. di Carlo, S. W. Graves and M. Toner, *Analytical Chemistry*, 2010, **82**, 3862–3867.
- 20 W. Lee, H. Amini, H. A. Stone and D. Di Carlo, *Proceedings of the National Academy of Sciences of the United States of America*, 2010, **107**, 22413–22418.
- 21 D. Di Carlo, *Lab on a Chip*, 2009, **9**, 3038.
- 22 H. Amini, W. Lee and D. Di Carlo, *Lab on a Chip*, 2014, **14**, 2739–2761.
- 23 W. Tang, S. Zhu, D. Jiang, L. Zhu, J. Yang and N. Xiang, *Lab on a Chip*, 2020, **20**, 3485–3502.
- 24 K. Hood, S. Kahkeshani, D. Di Carlo and M. Roper, *Lab on a Chip*, 2016, **16**, 2840–2850.
- 25 C. C. Chang, Z. X. Huang and R. J. Yang, *Journal of Micromechanics and Microengineering*, 2007, **17**, 1479–1486.
- 26 Q. Koziol and D. Robinson, *USDOE Office of Science*, 2018, <https://doi.org/10.11578/dc.20180330.1>.

- 27 Petre. Stoica and R. L. Moses, *Spectral analysis of signals*, Pearson/Prentice Hall, Upper Saddle River, N.J., 2005.
- 28 M. Hubert and S. van der Veen, *Journal of Chemometrics*, 2008, **22**, 235–246.
- 29 D. Arthur and S. Vassilvitskii, in *Proceedings of the eighteenth annual ACM-SIAM symposium on Discrete algorithms*, 2007, 1027–1035.
- 30 M. Herbig, A. Isozaki, D. di Carlo, J. Guck, N. Nitta, R. Damoiseaux, S. Kamikawaji, E. Suyama, H. Shintaku, A. R. Wu, I. Nikaïdo and K. Goda, *Nature Methods*, 2022, 1–2.
- 31 S. D. Hudson, *Rheologica Acta*, 2010, **49**, 237–243.